

# Evolution of galaxy dynamics over the last 10 Gyrs with MUSE/VLT

Master Thesis



**Author:** Mercier Wilfried

**Supervisor:** Contini Thierry

**Co-Supervisor:** Epinat Benoît

Observatoire de Paris

Institut de Recherche en Astronomie et Planétologie

Laboratoire d'Astrophysique de Marseille

May 28, 2019



# Abstract

# Contents

<b>1</b>	<b>Introduction</b>	<b>1</b>
1.1	Photometry and spectroscopy in galactic astronomy . . . . .	1
1.1.1	Photometric data . . . . .	1
1.1.2	Spectroscopy . . . . .	3
1.1.3	MUSE-VLT . . . . .	3
<b>2</b>	<b>Sample selection</b>	<b>4</b>
2.1	MUSE-GTO MAGIC . . . . .	4
2.2	COSMOS field . . . . .	4
2.3	Prior information on the galaxies . . . . .	5
2.3.1	Galaxies in structures . . . . .	5
2.3.2	Morphological information from COSMOS catalogues . . . . .	6
2.4	Checking catalogues values consistency . . . . .	7
2.4.1	Reasons for checking catalogues values . . . . .	7
2.4.2	Catalogues used for comparison . . . . .	8
2.4.3	Total magnitudes . . . . .	9
2.4.4	Morphological type classification . . . . .	10
2.4.5	Half-light radii . . . . .	12
2.5	SNR and size selection . . . . .	15
2.5.1	Size selection . . . . .	15
2.5.2	SNR selection . . . . .	18
2.6	Characterisation of the sample . . . . .	18
2.6.1	Selecting galaxies . . . . .	18
2.6.2	Redshift distribution . . . . .	20
2.6.3	Mass-SFR relation . . . . .	20
<b>3</b>	<b>Kinematical modelling</b>	<b>22</b>
3.1	Cleaning . . . . .	22
3.2	Kinematical parametrisation . . . . .	23
3.3	Model . . . . .	24
	<b>References</b>	<b>25</b>
<b>A</b>	<b>Details about morphological classification</b>	<b>28</b>
A.1	Non-parametric values . . . . .	28
A.1.1	Concentration . . . . .	28
A.1.2	Asymmetry . . . . .	29
A.1.3	Gini coefficient . . . . .	29

## List of Figures

1	Error on inclination as a function of $b/a$ and its error. . . . .	7
2	Comparison between magnitudes . . . . .	9
3	Morphological types comparison . . . . .	11
4	Comparison between half-light radii . . . . .	13
5	Comparison between radii against disk/bulge radius . . . . .	14
6	PSF FWHM variation with wavelength. . . . .	16
7	Selected sample . . . . .	19
8	Redshift distribution . . . . .	20
9	SFR-mass relation . . . . .	21

## List of Tables

1	Main characteristics of the observed MUSE fields . . . . .	4
---	--	---

# 1 Introduction

## 1.1 Photometry and spectroscopy in galactic astronomy

### 1.1.1 Photometric data

Photometric and spectroscopic data have been widely used in the past to study questions related to the formation and evolution of galaxies at both low and high redshifts. Photometry is a key component in the study of galaxy light profiles and the location of the different stellar populations.

Assuming the galaxies are resolved enough within the images, photometry gives us information about their morphological properties and can tell us how their content is distributed within them. Observations in different wavelength ranges (bands) give us insight into the differences in distribution between young and old stars (observed respectively in UV and near IR rest-frame bands), which can in turn indicate the presence of HII regions<sup>1</sup> (citation here). Typical wavelengths of observation include the visible spectrum, IR and UV. Ground based near-IR (NIR) photometry can also give information on the distribution of gas and old stars, and space based telescopes observing in the far-IR (FIR) can give us insight into the location of dust. Being able to determine the amount of dust along the line of sight, the so called column density defined as the 3D density integrated along the line of sight, is most important as it is mandatory to derive any robust estimates of absolute magnitude and Star Formation Rate (SFR).

Photometric information of galaxies is generally obtained through model fitting of the measured light profile, though other methods exist involving growth of ellipses (cite here).

The most commonly used model of galaxy shape, excluding more complicated cases such as irregular structures and merging galaxies, is a Sérsic profile which we generally write as (Graham et al., 2005)<sup>2</sup>

$$I(r) = I_e e^{-b_n \left( \left( \frac{r}{R_e} \right)^{1/n} - 1 \right)} \quad (1)$$

where  $r$  is the radial distance to the morphological centre of the galaxy,  $n$  is referred as the Sérsic index of the galaxy,  $R_e$  is the effective radius (also called half-light radius) which encloses 50% of the total luminosity of the galaxy,  $I_e$  is the intensity at the position  $R_e$  and  $b_n$  is a term which ensures that  $R_e$  does enclose half the total luminosity. The formal definition of  $b_n$  can be shown to be such that  $2\gamma(2n, b_n) = \Gamma(2n)$  with  $\gamma$  and  $\Gamma$  respectively the incomplete and complete gamma functions.

This equation can simplify into two famous galaxy profiles:

---

<sup>1</sup>Clumpy regions of ionised hydrogen with high values of star formation.

<sup>2</sup>The original definition  $I(r) \propto e^{(r/\alpha)^{1/n}}$  from Sérsic (1963) was modified to Eq. 1 because of the too small (immeasurable) values  $\alpha$  generally takes.

- an exponential disc for  $n = 1$  which represents a disk-like/spiral<sup>3</sup> galaxies
- a de Vaucouleurs profile for  $n = 4$  which describes elliptical (early-type) galaxies

This model with a freely varying Sérsic index is the one used in some morphology fitting software such as SExtractor (Bertin & Arnouts, 1996) or GIMD2D (Simard, 1998), but other forms can also be used from time to time. For instance one can use a combination of a bulge and a disk, with two fixed Sérsic indices instead of one allowed to freely vary, as in GALFIT (Peng et al., 2002).

Morphological parameters derived from the morphology modelling can then be used in various ways. We can classify the galaxies as elliptical or spiral using their Sérsic index or the most dominant feature between the disk and the bulge component if the modelling was a combination of both. We can also derive a value for the inclination of the galaxy on the sky using the ratio between the minor and major axes. Indeed, if we define the inclination of a galaxy as the angle between the normal to its plane and our line of sight, we have the relation

$$\cos i = b/a \quad (2)$$

where  $b$  is the galaxy minor axis and  $a$  its major axis.

If many photometric observations have been carried out on the same sky patch in multiple bands as in the case in the COSMOS field (see Section), different stellar populations and gas components can be observed. This gives us an approximate spectrum from which we can derive, for instance, a more precise photometric redshift than by combining a single instrument with multiple filters (insert citation here) and allows one to perform an SED fitting on this spectrum to derive other useful estimates such as the stellar mass, mean metallicity or star formation rate (citation here).

From both SED fitting and morphological parameters, it is then possible to derive scaling relations between them. For instance, we can derive the Tully-Fisher relation for late-type galaxies which relates the total luminosity of the galaxy with its maximum rotational velocity, or the Faber-Jackson relation for early-type galaxies where we use the velocity dispersion instead of the maximum rotational velocity (citation here).

The main drawback for having multiple band photometry is that it requires long observation times of the same sky area with different telescopes probing different wavelength ranges. Thus, it is not well suited to the study of galaxies' spectral features and therefore their kinematics.

---

<sup>3</sup>We will preferentially use the terms disk-like/late-type galaxies, with respect the Hubble sequence (Hubble, 1922), (Hubble, 1926), rather than spiral galaxies since many of the galaxies studied in the present work do show a disk morphology without clear spiral arm patterns.

### 1.1.2 Spectroscopy

On the other hand, astronomers have also been using spectroscopy to study galaxy chemistry, gas abundance and its kinematics. Contrary to photometry, these methods of observation do not yield an image of the galaxy but instead a spectrum of the pointed area. From such spectra, assuming we are able to unambiguously detect a spectral feature such as a ray ( $H\alpha$ ,  $H\beta$ , OII, OIII,  $Ly\alpha$ , etc.) or a line break (generally Lyman or Balmer break), we can infer a much more precise value for the galaxy redshift than in the photometry case as well as the gas velocity and its dispersion.

The lack of imaging implied that these methods only returned overall information on the whole galaxies or in specific regions chosen in advance for their scientific interest (HII region for instance). This was the case until slit spectroscopy was developed. Opposite to what has been previously said, slit spectroscopy give spectroscopic information not in a single pixel, but along a slit. Galaxies studied with this method generally relied on prior morphological information

Such data gives us information about how the gas moves inside the galaxies and allows one to classify the galaxies based on their kinematics (rotationally supported or dispersion dominated, see insert citation here).

In this context, it has become clear that a combination of these techniques would be necessary to better constrain the models of galaxy formation and to study in more details the origin of the observed scaling laws (SFR-mass, mass-size, luminosity-mass relations, etc.). In recent years, this has become possible with the advent of Integral Field Spectroscopy (IFS) astronomy. This technique combines the advantages of both photometry and spectroscopy by measuring the spectrum of each pixel in an image, yielding a 3D cube with two spatial and one spectral dimensions. Such instruments lacked for the most part a good spatial resolution until recently, but have now filled the gap.

### 1.1.3 MUSE-VLT

MUSE is an Integral Field Unit (IFU) mounted on the VLT in Chile which spans a  $1' \times 1'$  Field of View (FoV). Its wavelength range covers both the visual spectrum and the Near Infra-Red part (NIR), going from 4650 Å to 9300 Å. This instrument was built with the main purpose of performing blind searches of sources in the field. The wavelength range is well suited to detect the OII doublet in the redshift range 0.4, 1.4.



## 2 Sample selection

### 2.1 MUSE-GTO MAGIC

### 2.2 COSMOS field

Group ID <sup>1</sup>	Ra <sup>2</sup> J2000 (°)	Dec <sup>3</sup> J2000 (°)	Exposure <sup>4</sup> (hr)	Average seeing <sup>5</sup> (")	Total nb. galaxies <sup>6</sup>	Nb. field galaxies <sup>7</sup>
CGr32	NaN	NaN	$3 \times 4.35$	0.51 - 0.58	NaN	NaN
CGr34_d	149.87766	2.502331	5.25	0.63	NaN	NaN
CGr34_bs	149.87766	2.502331	4.75	NaN	NaN	NaN
CGr30_d	150.144225	2.065971	9.75	0.67	NaN	NaN
CGr30_bs	150.144225	2.065971	6.25	NaN	NaN	NaN
CGr84	150.057219	2.599744	5.25	0.59	NaN	NaN
CGr84-N	NaN	NaN	1	0.51	NaN	NaN
CGr114	149.994285	2.258044	2.2	0.68	NaN	NaN
CGr79	149.820686	1.821825	4.35	0.60	NaN	NaN
CGr28	150.218094	1.812667	1	0.62	NaN	NaN
CGr26	150.492767	2.069139	1	0.59	NaN	NaN
CGr61	149.728741	1.915987	1	0.64	NaN	NaN
CGr51	149.982756	1.801899	1	0.6 – 0.7	NaN	NaN
CGr23	149.790782	2.162648	1	0.68	NaN	NaN

Table 1: Main characteristics of the observed MUSE fields. Groups ending with \_d correspond to deep observations (full stacked OBs) and with \_bs correspond to best-seeing observations (only OBs with a seeing below 0.7"). The seeing is given for the [OII] wavelength at the group's redshift. 1. MUSE group number, 2. Group centre's right ascension, 3. Group centre's declination, 4. Duration of observations, 5. Average seeing during observation, 6. Total number of detected galaxies within MUSE FoV, 7. Number of field galaxies found by the FoF algorithm.

The point of the analysis is to perform a joint study of the morphology and the kinematics of field galaxies in COSMOS (Scoville et al., 2007) using respectively HST ACS images and MUSE data. To this end, a set of 12 galaxy structures (these can be either groups or clusters) in COSMOS was selected. The choice of the COSMOS field for this analysis was made because of the large number of multi-band photometric data available for the galaxies in this field and the presence of rich (large number of member galaxies) galaxy groups.

Guaranteed Time Observations (GTO) centred on the groups were performed from which 14 different MUSE Fields of View (FoV) of  $1 \times 1 \text{ arcmin}^2$  were obtained. Each is composed of Observation Blocks (OB) of **30 min** each with the Position Angle (PA) of the instrument rotated by  $90^\circ$  between consecutive observations.

Most of the groups are in one FoV, except for CGr32. Since this group is **larger** than

the others, three slightly overlapping FoVs were taken around it. A couple of groups were also split into *deep* and *best-seeing* observations, the former combining all the OBs regardless of the average seeing in each OB, when the latter only kept OBs with an average seeing higher than  $0.7''$ .

The main characteristics of the observed FoVs, including the position of their centre, the exposure per FoV, the average seeing during the observation, the total number of galaxies and the number of field galaxies detected by the FoF algorithm are listed in Table 1.

These structures were chosen within the COSMOS field. This ensured them to have both a large set of corresponding photometric data available from Laigle et al. (2016) catalogue and HST images with a much better resolution ( $0.03 \text{ arcsec/px}$  for HST and  $\sim 0.2 \text{ arcsec/px}$  for MUSE). A few galaxies in CGr30\_deep and around some stars might have also been detected within the data cubes but not in HST images. In the former case, the reason is that a blind source detection was performed with ORIGIN (Bacon et al., 2017) which can deblend sources even below the PSF. For the latter, this is because galaxies were detected in areas around stars which were masked when creating Laigle et al. (2016) catalogue.

## 2.3 Prior information on the galaxies

### 2.3.1 Galaxies in structures

This internship was planned to be similar in many aspects to what has done V. Abril-Melgajero in LAM, Marseille. She studied the morphology and the kinematics of the galaxies within the structures observed by MUSE in COSMOS. The galaxies were therefore found in the same MUSE fields as those we are using in this work, but belong to structures instead of being labelled as **field galaxies**.

To differentiate between group and field galaxies, a Friend of Friends algorithm (FoF) was run prior to my arrival on the galaxies in each MUSE field. Thus, each galaxy was labelled either as belonging to a structure or as field galaxies.

Additionally, a morphological analysis had already been performed by V. Abril-Melgajero with GALFIT on galaxies in structures. Two Sérsic profiles with fixed Sérsic indices ( $n = 1, 4$ ) were used to describe these galaxies as a combination of a disk and a bulge component. Hence, their intensity can be written as

$$I(r) = I_{e,d} e^{-b_1 \left[ \frac{r}{R_d} - 1 \right]} + I_{e,b} e^{-b_4 \left[ \left( \frac{r}{R_b} \right)^{1/4} - 1 \right]} \quad (3)$$

where  $I_{e,d}$ ,  $I_{e,b}$  are the effective intensities of the disk and the bulge component respectively and  $R_d$ ,  $R_b$  their half-light radii.

Therefore, we already had morphological information for roughly half of the total sample including model parameters as described above, but also morphological parameters such as the ellipticity of the galaxies, the Position Angle (PA) of their kinematical main axis (which can be different from the morphological PA).

### 2.3.2 Morphological information from COSMOS catalogues

The total number of galaxies detected by MUSE in COSMOS is around 1000. Roughly half of them belong to structures and the other half are labelled as field galaxies. Among these galaxies, not all of them are useful to our study. Some may be too close to the edge, others be too noisy with a low Signal to Noise Ratio (SNR), or too small for any relevant kinematical modelling. It is thus mandatory to apply a selection on our data set of field galaxies, first to save time for the analysis, but also to reduce uncertainties.

Our goal is to perform a joint study of the morphology and the kinematics of these galaxies. The tools and the models for the kinematical modelling were already developed as they were used by V. Abril-Melgajero. On the other hand, fitting morphological models with software such as GalFit or SExtractor would have required additional time which we did not have. Hopefully for us, morphological modelling had already been performed on the galaxies in the COSMOS field, so we could focus on the kinematical part.

Morphological information for all the galaxies in COSMOS can be found in various catalogues and tables<sup>4</sup>. To start with, we decided to use the two most complete catalogues we could find, that of Tasca (maybe citation) and Cassata (maybe citation as well). Both catalogues contain morphological information including the central position of the galaxy, its half-light radius, concentration and asymmetry parameters, ellipticity, Position Angle of the major morphological axis (PA), and many more for roughly 232000 galaxies. The authors obtained morphological information by running SExtractor on HST images of the galaxies in Laigle et al. (2016) catalogue.

Since we already had data from Laigle et al. (2016) for our galaxies, we only had to cross-match our table with Cassata's and Tasca's catalogues to collect their morphological parameters. We decided to cross-match our data with each catalogue separately and then with both using the right ascension  $\alpha$  and declination  $\delta$  of the centre of the galaxies, allowing for a maximum separation between the MUSE source and the closest source within Cassata's and Tasca's catalogues of 1 arcsec maximum.

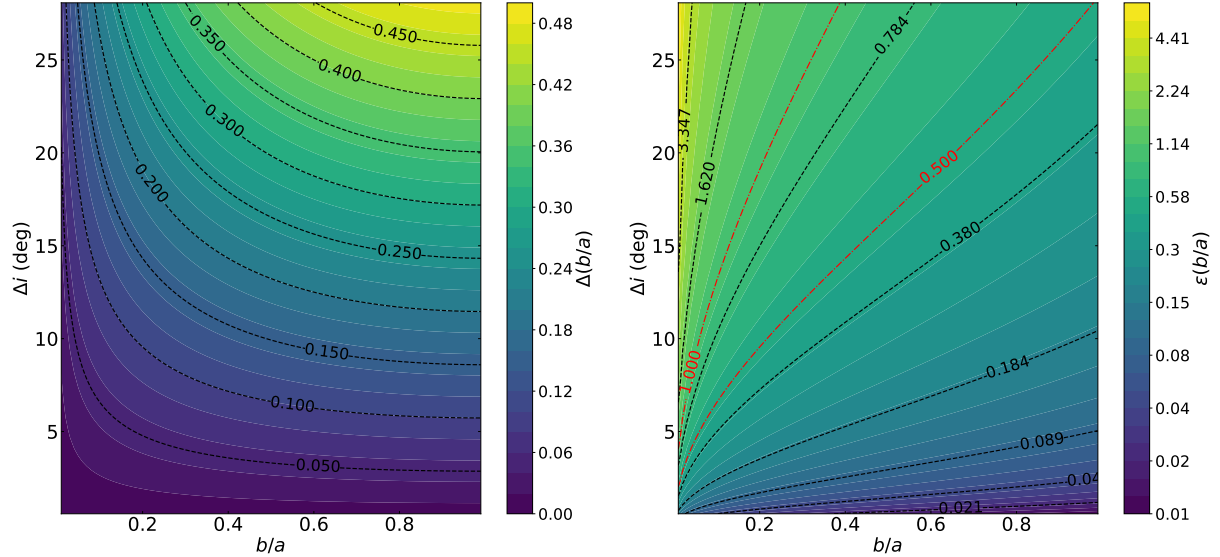
This cross-matching procedure was performed for both field and structure galaxies. The reason for cross-matching cluster galaxies when we are only interested in those in the field will be discussed in the following section.

---

<sup>4</sup><https://irsa.ipac.caltech.edu/data/COSMOS/tables/morphology/>

## 2.4 Checking catalogues values consistency

### 2.4.1 Reasons for checking catalogues values



(a) Error on inclination as a function of  $b/a$  and its absolute error. Contours of  $\Delta(b/a)$  are plotted in black dashed lines with their corresponding value.

(b) Error on inclination as a function of  $b/a$  and its relative error. Contours of  $\epsilon(b/a)$  are plotted in black and red dashed lines with their corresponding value.

Figure 1: Error on inclination as a function of  $b/a$  and its error. Left: as a function of the absolute error on  $b/a$  ( $\Delta(b/a)$ ). Right: as a function of the relative error on  $b/a$  ( $\epsilon(b/a)$ ). Red contours correspond to values for which there is a 50% and 100% error on  $b/a$ .

As a first step, we must select a sample based on relevant criteria. This is meant to ensure us to have reliable morphological and kinematical parameters and to reduce statistical errors. Given that any kinematical modelling relies on prior morphological information (galaxy centre, ellipticity, PA), we can only use a combination of values derived from spectral fitting, for instance the Signal to Noise Ratio (SNR) as described in Eq. ??, and morphological modelling such as a measure of a galaxy radius to select our sample.

Before this internship, spectral fitting on the integrated spectra of the galaxies had already been done, and we combined our data with morphological information from COSMOS catalogues as discussed in the previous section. Potentially useful morphological information included half-light radii, magnitudes, ratios of minor to major axis ( $b/a$ ) or equivalently a measure of the ellipticity of the galaxies. Nevertheless, using this data without checking first how well it compares to values found in other catalogues and/or derived using different softwares/models could lead to high biases and uncontrolled errors. Thus, before discussing any selection criteria for our sample, we must first assess the reliability of the parameters we are going to use in later sections.

Important values to check are the half-light radius, as it will be used to select our sample, the  $b/a$  ratio and the PA since these are prior information for the kinematical modelling. We also checked that there was a correlation between GALFIT and the catalogues magnitudes. The axes ratio has a crucial importance since it is directly related to the inclination of the galaxy on the sky through Eq. 2. Given a certain error  $\Delta(b/a)$ , and using the usual formula for computing the error  $\Delta f = |\partial_x f| \Delta x$  of a function  $f$ , we find for the inclination

$$\Delta i = \Delta(b/a) \left| \frac{b}{a} \left( 2 - \frac{b}{a} \right) \right|^{-1/2} \quad (4)$$

This is illustrated in Fig. 1 where  $\Delta i$  has been plotted as a function of  $b/a$  and its error (absolute on the left, relative on the right). Contours of the error on  $b/a$  have been over-plotted to show how evolves  $\Delta i$  given a fixed error on  $b/a$ . As expected, the higher the error on  $b/a$  the higher the error on  $i$ . An error as high as 50% could yield  $\Delta i \approx 27^\circ$ , though this value is reached for  $b/a \approx 1$  where the axes ratio is the least constrained by the morphology. A more appropriate error on  $b/a$  of 20% gives a maximum  $\Delta i$  slightly above  $10^\circ$ , which is correct.

Since the inclination affects the galaxy maximum rotational velocity, and so potentially on the classification of galaxies as rotationnaly supported or dispersion dominated (see Section insert ref here), this indicates us that for any proper kinematical modelling we must check carefully that the values of axes ratios are consistent between catalogues.

#### 2.4.2 Catalogues used for comparison

As stated in previous sections, we cross-matched our catalogue of galaxies detected by MUSE in COSMOS with Cassata's and Tasca's, two tables with morphological information for the galaxies in Laigle et al. (2016).

However, as can be seen in Fig. 4 and 5, we found large discrepancies between the parameters. Thus, to better understand their origin, we chose to cross-match our catalogue with another one (also based on Laigle et al. (2016)) from Zurich. This table has fewer HST counterparts of MUSE galaxies than in the other two but it contains additional morphological information which we can use for the comparison.

In addition to that, we already had GALFIT morphological information on  $\sim 500$  group galaxies with strong confidence in their value. Therefore, we chose to compare the data in the three morphological catalogues based on Laigle et al. (2016) with that of GALFIT.

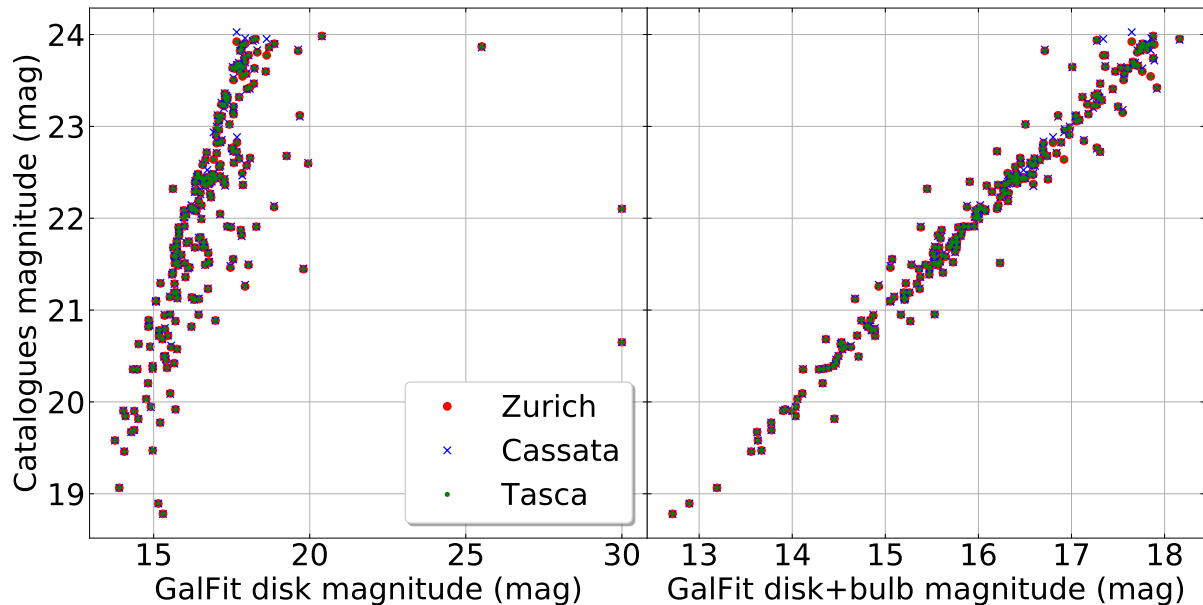


Figure 2: Comparison between the morphological catalogues magnitudes and that of GALFIT for cluster galaxies. Magnitudes from the catalogues agree well between each other. Left: compared with GALFIT disk magnitude only. The slope is too high and a few points are scattered far from the line. Right: compared with the total GALFIT magnitude as defined in Eq. 7. We find a good linear relation with **poor scatter**.

### 2.4.3 Total magnitudes

The first value we can easily compare is the total magnitude. Cassata's, Tasca's and Zurich's catalogues provide a measure of the total magnitude derived from fitting with SExtractor a single Sérsic profile with a free Sérsic index  $n$  on HST images.

Given that GALFIT light profile was modelled using two Sérsic profiles with fixed Sérsic indices ( $n = 1, 4$ ), we had two measures of the magnitude of these galaxies: one for the bulge component  $m_b^{\text{GF}}$ , and another for the disk component  $m_d^{\text{GF}}$ . To have a meaningful comparison between magnitudes, we need to compute the GALFIT total magnitude by combining the bulge and the disk components. Both are defined as

$$m_i^{\text{GF}} = -2.5 \log_{10} (F_i^{\text{GF}}) + C \quad (5)$$

where  $i = b, d$  represents either the bulge or the disk,  $F = L/4\pi D^2$  is the flux of the galaxy in some band,  $L$  its intrinsic luminosity,  $D$  its cosmological luminosity distance to us and  $C$  a constant depending on the band used.

Considering that the two components have different luminosities but are located at the same distance, we can add the fluxes together. Thus the total GALFIT magnitude can also be written as

$$m_{\text{tot}}^{\text{GF}} = -2.5 \log_{10} (F_b^{\text{GF}} + F_d^{\text{GF}}) + C \quad (6)$$

Inverting Eq. 5 to get the components flux as a function of their magnitude and inserting it into Eq. 6 yields

$$m_{\text{tot}}^{\text{GF}} = -2.5 \log_{10} \left[ 10^{-\frac{m_b}{2.5}} + 10^{-\frac{m_d}{2.5}} \right] \quad (7)$$

This is the value that should be compared with the three catalogues magnitudes. Fig. 2 shows how these scale with each other and with GALFIT disk magnitude on the left, and the total magnitude from Eq. 7 on the right. As expected, the catalogues give the same value except for a few points. We see that the total GALFIT magnitude gives a much better, poorly scattered linear relation with the catalogues magnitudes. Even though there is an offset between GALFIT and the catalogues, this is due to using different conventions for the constant term in Eq. 5.

The same comparison was done on field galaxies, except we did not have GALFIT magnitudes in this case. We also found a good agreement between the catalogues magnitudes.

#### 2.4.4 Morphological type classification

We might expect to have some discrepancies in our data because of the models used between GALFIT and SExtractor/GIM2D. A way to check this effect is to study how these differences scale with the morphological type of the galaxies. For instance, if we use the disk half-light radius of GALFIT to compare with that of SExtractor, we might expect to have some scatter in our relation for the elliptical galaxies as the disk component is not the best one to describe them.

To see how these relations scale with morphological types, we can use the classification given in the three morphological catalogues. These classifications are based on methods which can be quite different and which can use morphological parameters in different ways. A more detailed explanation of the parameters used, of how these methods work, of their strength and weaknesses can be found in Appendix A. We provide below a short introduction to these classifications:

- Cassata’s catalogue gives a classification based on morphological parameters they derived with SExtractor. To do so, they use a reference of 500 galaxies with known parameters which they visually classify as either elliptical, disk-like/spiral or irregular. From this set, each time a new galaxy must be classified, its 11 closest neighbours are inspected and the most frequent class is assigned to the galaxy.
- Tasca’s catalogue gives different classifications based on three methods. The first one is similar to the one used by Cassata. This is also the classification they recommend to use because this is the one they put the more their trust in. The second one uses

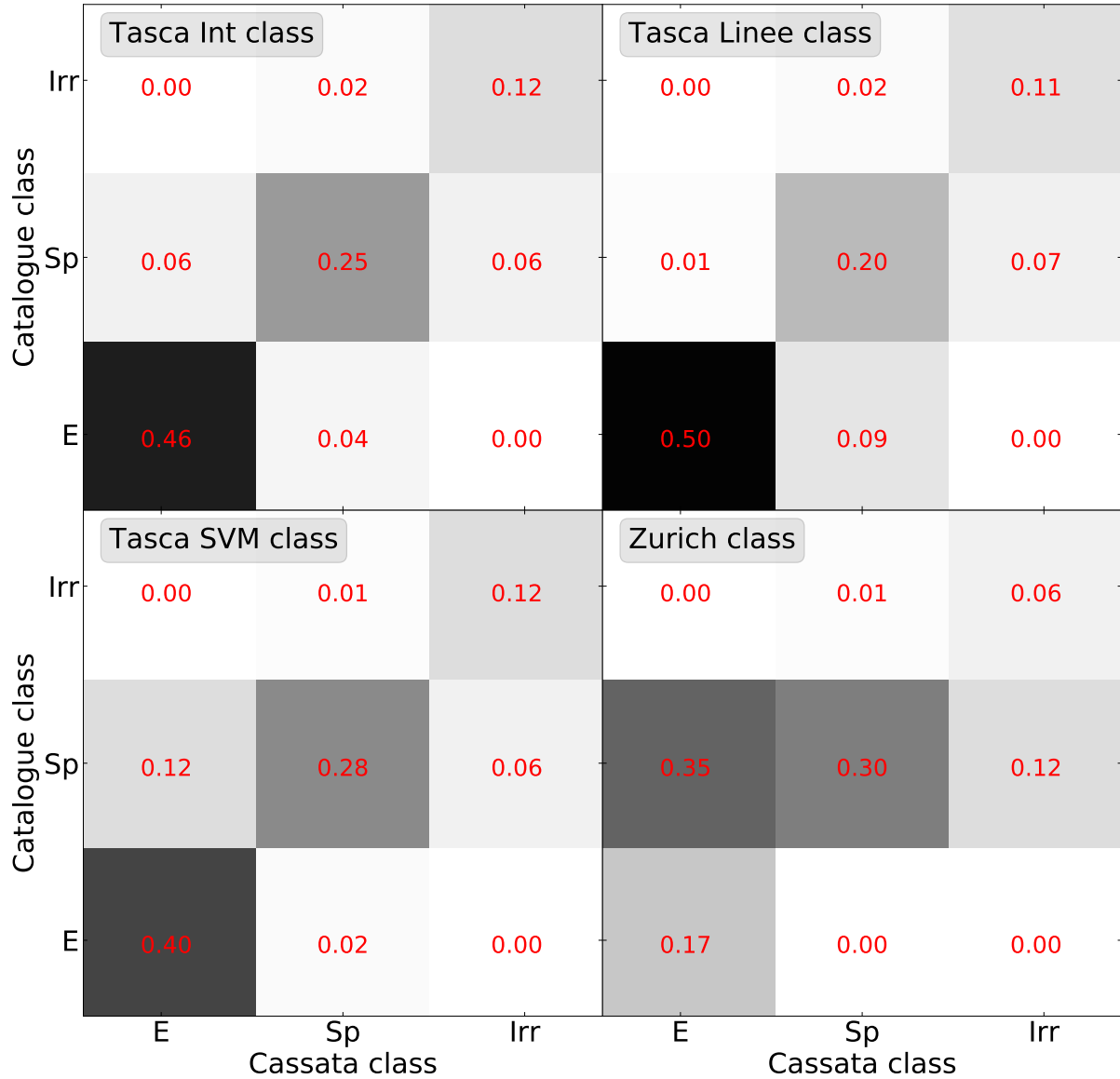


Figure 3: Comparison between morphological types given in Tasca and Zurich catalogues against that of Cassata. The three classifications of Tasca are those described in Section 2.4.4. Galaxies are labelled as follows: E for ellipticals, Sp for spirals/disks-like, Irr for irregulars. The percentage of galaxies falling into the given classes is indicated in red and the method compared with Cassata's is shown on the top left corner of each plot. We find good agreement between Tasca and Cassata types but not between Cassata and Zurich.



the technique described in (insert Abraham 1996 here) using the asymmetry and concentration parameters. The last one uses a support vector machine to classify galaxies.

- Zurich’s catalogue gives a single classification called Zurich Estimator of Structural Type (ZEST) which is described in (Scarlata et al., 2007). This method is based on a Principal Component Analysis (PCA). They decided to keep the first three Principal Components (PA) which retain most of the information present in the original five parameters (concentration, asymmetry, Gini coefficient, second-order moment of the brightest pixels producing 20% of the total flux and the ellipticity of the galaxy).

The morphological types given in Tasca’s and Zurich’s catalogues are compared against the class given by Cassata in Fig.3. We observe a good agreement between Cassata’s and Tasca’s types with just a few elliptical galaxies labelled as disk-like and vice versa. Roughly 50% of the galaxies appear to be elliptical. On the contrary, Zurich’s classification seems to label more than 70% of the galaxies as disk-like, including a large number of elliptical galaxies .

Considering the recommendation of Tasca to use its Int class and since we find a good agreement between Cassata’s morphological type and those given by Tasca, we decided to use and to stick to Cassata’s class throughout this work whenever we needed to separate galaxies between elliptical/disk-like/irregulars. This choice also ensured us to have the largest sample possible with a coherent classification as Cassata’s catalogue is the one with the largest number of HST counterparts of MUSE galaxies in the COSMOS field. Because of the incompatible results between Zurich’s and Cassata’s/Tasca’s types, we decided to put aside these values and not use them, though this shall require further investigation in future work to assess the origin of these discrepancies.

#### **2.4.5 Half-light radii**

One of the most important parameters we have to check before the selection is the half-light radius of our galaxies. Indeed, if we underestimate it, we might remove from our sample resolved galaxies and therefore reduce our statistics. On the other hand, overestimating it would give us too many unresolved galaxies for which we would spend time performing the cleaning routine without being able to perform their kinematical analysis in the end.

Hence, it is mandatory to thoroughly check the values of the half-light radius from the three catalogues against that of GALFIT, and understand the origin of any discrepancies if there happens to be some.

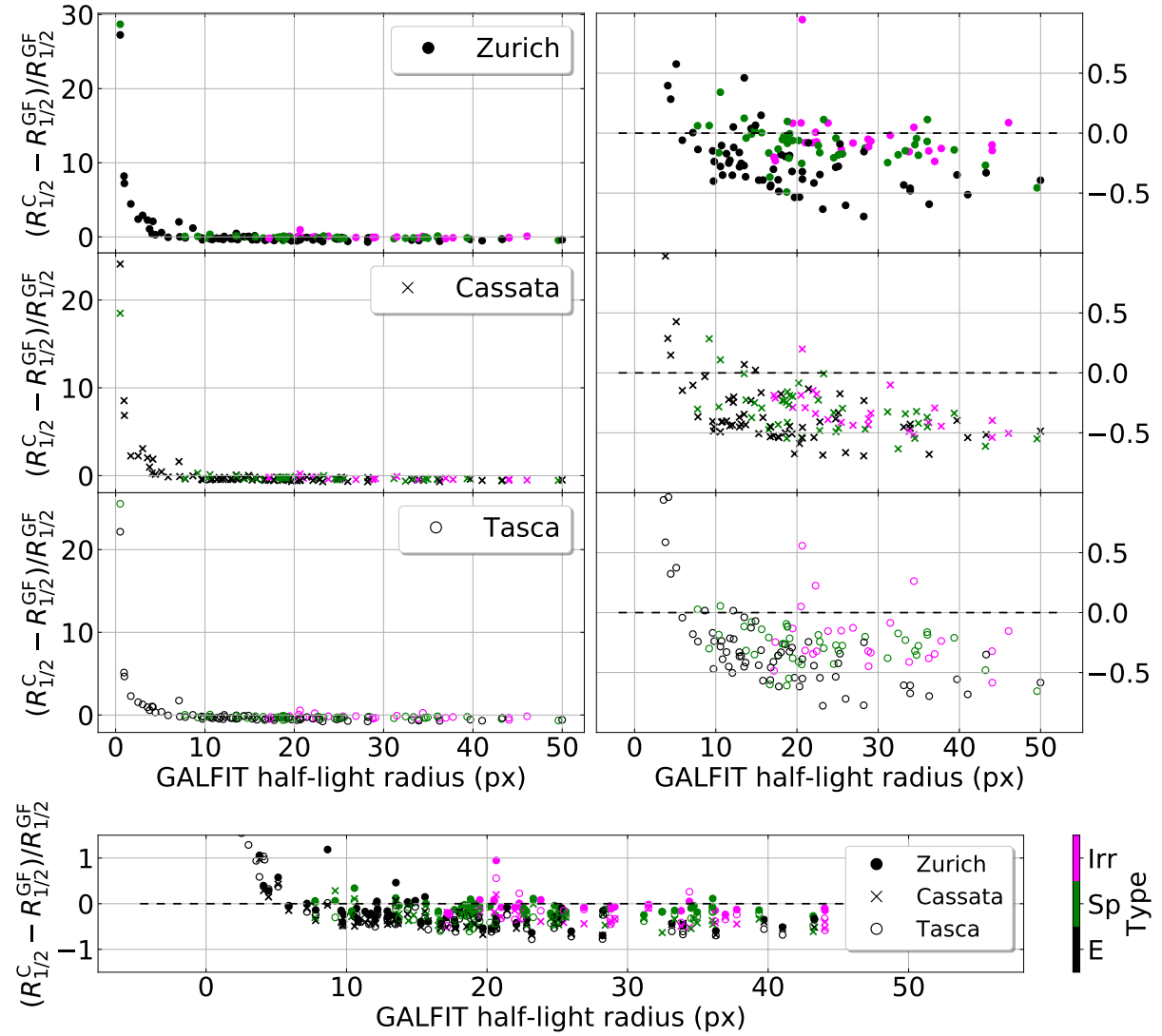


Figure 4: Comparison between half-light radii from the morphological catalogues and the radius of GALFIT disk component. The relative error is shown for the three catalogues (from top to bottom, Zurich, Cassata and Tasca). Points have been colour coded according to their classification given in Cassata's catalogue (Irr for irregular, Sp for spiral/disk, E for ellipticals). Left: the full range is plotted. Right: a zoom on the points with  $R_{1/2}^{GF} \geq 5$  px. The last plot on the bottom combines the information within the three plots on the left.

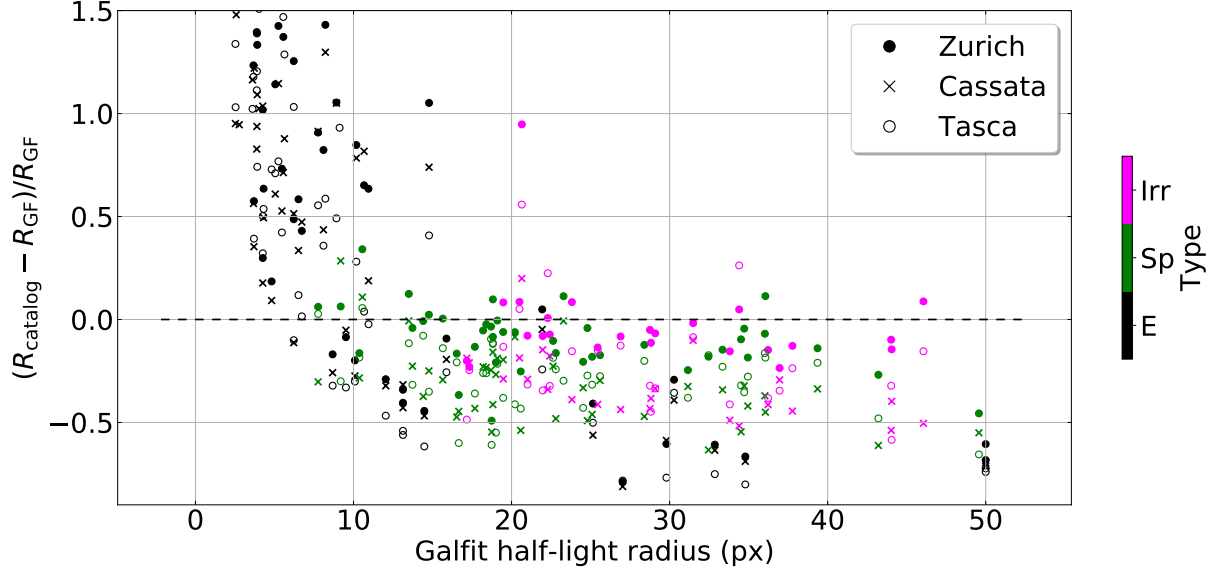


Figure 5: Comparison between catalogues radii and that of GALFIT. This figure is similar to Fig. 4 but we use GALFIT bulb radius for elliptical galaxies. The catalogues appear to overestimate the elliptical galaxies radii when using GALFIT bulge radius.

We found a quite large disagreement between our GALFIT half-light radius and those given in the morphological catalogues, as well as among them. This is illustrated in Fig. 4 where the half-light radii in the catalogues are compared against that of GALFIT. Galaxies are colour coded according to the classification given in Cassata’s catalogue. We checked that using Tasca’s classifications as described in Sec. 2.4.4 did not change our conclusions. In these plots, we decided to use for the x-axis the half-light radius of the GALFIT disk component for all the galaxies, even though we might expect the ellipticals to be better described by their GALFIT bulge half-light radius.

The catalogues radii seem to be overestimated with respect to that of GALFIT for low  $R_{1/2,d}^{GF}$ . This was expected as catalogues half-light radii are computed using SExtractor. Since it does not take into account the PSF in its fitting routine, we expect the PSF to dominate more for galaxies with small angular sizes. On the contrary, GALFIT does take into account the PSF in its calculations and therefore we expect the half-light radius of GALFIT to be smaller than SExtractor’s when reaching low values of  $R_{1/2,d}^{GF}$ .

When focussing on galaxies with a GALFIT radius larger than the HST-ACS PSF FWHM which is around  $\sim 0.15''$  ( $4 - 5$  px), we observe a global underestimation for all the catalogues, up to roughly 50%. This scatter is mainly due to elliptical galaxies. On the contrary, radii of disk-like galaxies have the least scatter and bias, especially the values given in Zurich’s catalogue. This different behaviour between elliptical and disk-like galaxies might be explained, as mentioned above, by the fact we are using the half-light radius of GALFIT disk component to assess the reliability of the elliptical galaxies half-light radii from the catalogues. This is probably not the best choice, and a better may be to use the bulb components, which better describes the light profile of an elliptical galaxy,

and its half-light radius to study elliptical galaxies.

If we decide to split the galaxies into two categories, ellipticals and disks/irregulars, and if we use for the first category  $R_{1/2,b}^{\text{GF}}$ , and for the second  $R_{1/2,d}^{\text{GF}}$  we find that elliptical galaxies half-light radii in the catalogues are now overestimated as shown in Fig. 5. This result, and the underestimated values when using the disk radius for the elliptical galaxies, indicates us that elliptical galaxies seem to be neither dominated (in terms of radius) by the disk component, nor by the bulge in the GALFIT model. It is thus necessary to directly compute an overall half-light radius by integrating the galaxies light profile given in Eq. 3

CONCLURE SUR QUEL PARAMETRE UTILISER ET QUELLE CORRECTION APPORTER.

## 2.5 SNR and size selection

### 2.5.1 Size selection

Since we are interested in keeping well resolved field galaxies, we need to apply relevant criteria in order to select the right galaxies. The most obvious parameter we can use to make our selection is the size of the galaxy. We already checked in Section 2.4.5 biases which might arise and their origins, and we corrected them whenever possible. Thus, we only need to define a size criterion to select our sample.

Following the earlier work done in Bacon et al. (2015) and Bacon et al. (2017), the MUSE Point Spread Function (PSF), that is the pattern we obtain when we observe a point-like source with MUSE, is most well described by a Moffat (1969) profile

$$I_{\text{PSF}}(r) = I_0(1 + (r/\alpha)^2)^{-\beta} \quad (8)$$

where  $r$  is the radial distance to the centre and  $\alpha, \beta$  are two seeing dependant parameters. In our case, we are interested in the Full Width at Half Maximum (FWHM) since it is directly related to the seeing conditions and since it gives us information about the minimum spatial extent within which we start to loose information. The FWHM can be easily derived from the equality  $I_{\text{PSF}}(\text{FWHM}/2) = I_0/2$  using Eq. 8, from which we get the following relation

$$\text{FWHM} = 2\alpha\sqrt{2^{1/\beta} - 1} \quad (9)$$

According to the aforementioned articles the value of  $\beta$  is expected to remain roughly constant and, additionally, we would expect from differential image motion theory (in-

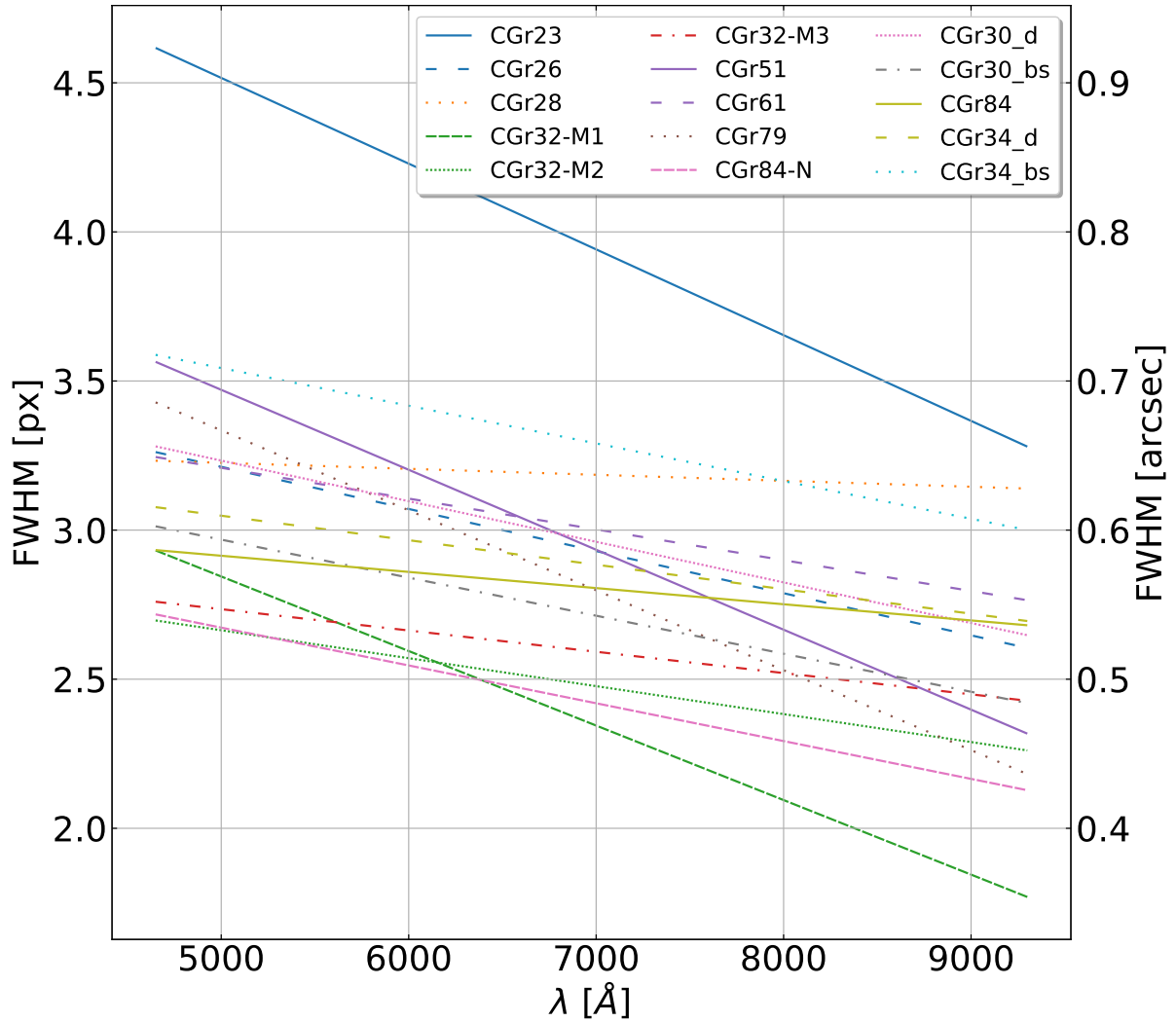


Figure 6: PSF FWHM variation with wavelength for the 13 FoVs as measured by Valentina. At least two values of the FWHM were derived from stars in the FoVs by fitting a Moffat distribution to their light profile. We assumed a linear evolution with wavelength. Strong fluctuations appear depending on the observed FoV.

sert this paper here when read 10.1086/342683) the FWHM to linearly decrease with wavelength.

All galaxies are observed via their [OII] doublet at the same rest-frame wavelength. But, given that they are all field galaxies located at a different redshift  $z$ , we actually observe them at wavelengths covering the entire MUSE spectrum, that is we have the usual relation

$$\lambda_{\text{obs}} = \lambda_{\text{em}}(1 + z) \quad (10)$$

where  $\lambda_{\text{em}}$ ,  $\lambda_{\text{obs}}$  are respectively the emitted (rest-frame) and observed wavelengths. Therefore, there is not only one FWHM value per field (the FWHM will also vary with MUSE fields as seeing conditions change from date to date), but one per galaxy, which we

can derive if we know the two parameters (slope and offset) which characterise the linear evolution of the FWHM with wavelength. To derive this relation, we need at least two measures of the FWHM at two different wavelengths per field. Assuming seeing conditions are similar within a field (no spatial dependence), we can use the same linear relation per MUSE field to compute the FWHM for the [OII] wavelength at the redshift of the galaxy.

As discussed above,  $\beta$  should remain constant, which means the FWHM is entirely described by the parameter  $\alpha$  through Eq. 9. The measure of  $\alpha$  had already been done by V. Abril-Melgarejo on at least two stars per field. For each star, two measures of  $\alpha$  were computed by fitting a Moffat profile onto their [OII] and [OIII] images at the redshift of the observed structure (see Table 1).

Though a more rigorous modelling of the wavelength variation of the PSF FWHM including both more data points and potentially higher order terms is mandatory for future analysis, we decided to stick to this values in the present work, keeping in mind the large uncertainties which will affect the velocity dispersion maps in the modelling section. A representation of the FWHM variation with wavelength for 15 out of 16 observations is shown in Fig. 6. We only have missing values of the FWHM for CGr114. Most MUSE fields have FWHM values below  $0.7''$  which is not surprising given that it was one of the constraints of the observations. CGr23 is the only FoV to have its FWHM above  $0.7''$  for almost every wavelength. Only galaxies further than  $z \approx 1.11$ . In Table. 1, the seeing is the average over the OBs for the [OII] doublet at the redshift of the group which is around 1.17. Hence the value below  $0.7''$ .

Considering that the FWHM is a measure of how spread a point-like source is, and since we are interested in working with resolved enough galaxies in order to better constrain their kinematics, we would like galaxies to have a characteristic size at least above the FWHM. Given that for almost all the fields we have an upper limit on the FWHM of about  $0.7''$ , we decided to use this upper limit as our size selection criterion

$$R_{1/2} \geq 0.35'' \approx \text{FWHM}/2 \quad (11)$$

Moreover, according to Swinbank et al. (2017) who compared the half-light radius of the nebular [OII] emission in MUSE images with that of their HST counterpart in ACS *I* or WFC *H*-band, the [OII] half-light radius seems to scale with the HST radius as

$$R_{1/2}^{\text{OII}} = (1.18 \pm 0.03) R_{1/2}^{\text{HST}} \quad (12)$$

Thus, we expect the galaxies in the MUSE images to be larger than their HST counterparts, which means our choice of lower limit for the morphological radius in our sample should eliminate most of the unresolved galaxies. Though, we also risk to eliminate re-

solved galaxies in our selection.

### 2.5.2 SNR selection

The other information we can use to select our sample is the Signal to Noise Ratio (SNR), which tells us how well our galaxy is detached from the background. The SNR is generally derived as the ratio between the source's signal and the background level. The noisier an image, the lower the SNR is.

As explained in later sections, the galaxies must be automatically and then manually cleaned before fitting a kinematical model on the velocity maps in order to remove any pixel dominated by noise which might compromise the fit. One of the criteria used by the routine to decide whether a pixel belongs to the galaxy is a lower limit on the SNR of pixel (typically 5). Thus, if we want to have enough detection in our cleaned maps to perform the kinematical modelling, we must select galaxies with a strong enough SNR.

In our case, PLATEFIT, described in ), was run on the integrated spectrum of the galaxies in order to derive their spectral features. From the parameters returned by CAMEL, we used the [OII] flux and its error to derive the SNR as

$$\text{SNR} = \frac{[\text{OII}] \text{ flux}}{[\text{OII}] \text{ flux error}} \quad (13)$$

This is the [OII] SNR from the integrated galaxy spectrum computed using pixels within data cubes restricted around the galaxy. Since the typical SNR value used by the routine to clean the maps is around 5, we decided as a first step to choose an SNR lower limit of 10, allowing us to keep galaxies with strong enough detection after the automatic cleaning is performed.

## 2.6 Characterisation of the sample

### 2.6.1 Selecting galaxies

We decided to visually inspect galaxies around the SNR and the size cuts to quantify (a) how many resolved galaxies would be lost if we applied the criteria given in Sec. 2.5.1 and 2.5.2 (false negative) (b) how many unresolved galaxies would be selected in our sample (false positive). To do so, we defined four boxes:  $5 \leq \text{SNR} \leq 10$ ,  $10 \leq \text{SNR} \leq 15$ ,  $0.25'' \leq R_{1/2} \leq 0.35''$  and  $0.35'' \leq R_{1/2} \leq 0.45''$  containing respectively 46, 20, 58 and 49 galaxies. We then ran the automatic cleaning routine on all the galaxies in these boxes. After visually inspecting their size in the cleaned maps, we classified them as resolved or not. These boxes and the SNR, half-light radius and redshift of the full sample of field galaxies before selection are shown in Fig.7.

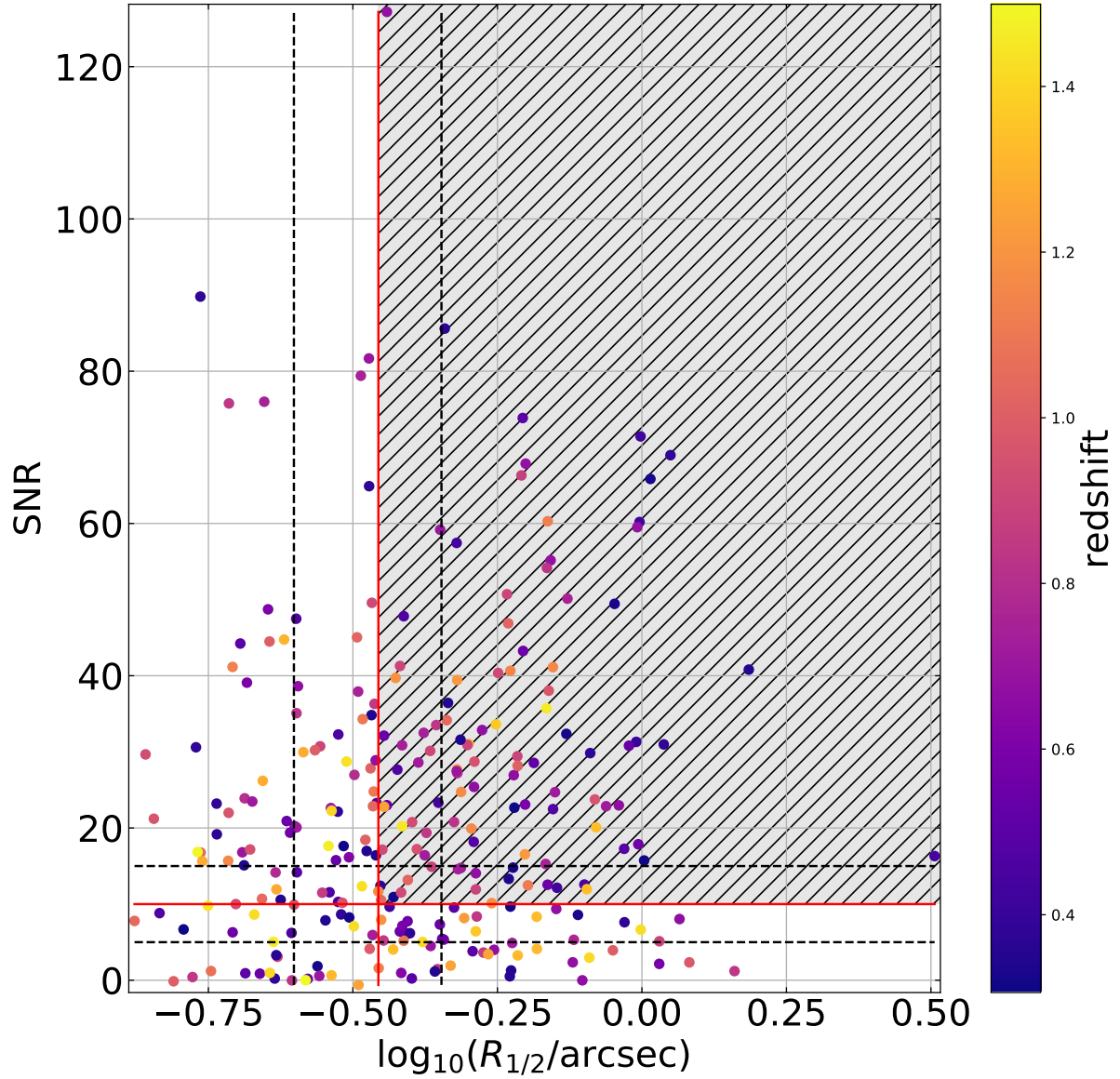


Figure 7: Full sample of 261 field galaxies with our selection box over-plotted (hatched area). Galaxies with  $5 \leq \text{SNR} \leq 15$  and  $0.25'' \leq R_{1/2} \leq 0.45''$  (bounds plotted as dashed lines) were visually inspected to check how many resolved galaxies we might have loosed. Selection criteria from Sec. 2.5 are also plotted as solid red lines. No specific trend appear with redshift.



Among the 261 field galaxies, 103 fall into the limits imposed in Sec.2.5. We find that roughly 26% of the galaxies below the cuts are actually false negatives and that 15% above them are false positives. Since this classification is purely visual, slightly relaxing the constraints on when a galaxy is resolved or not allow these values to vary by roughly 10%. Hence, it seems our choice of lower bounds for the SNR and the half-light radius is fine, though in future works we might increase our sample by a factor of  $\sim 1.5$ .

### 2.6.2 Redshift distribution

The choice of the [OII]  $\lambda\lambda 3729, 3729 \text{ \AA}$  doublet for the kinematical analysis was due in part to the large range of redshift it covered given the MUSE observed wavelengths. We therefore had in our catalogue galaxies spanning a redshift range from 0.3 to about 1.4. As show in Fig.8, after our selection we loose the majority of the most distant galaxies as well as a significant fraction of galaxies with  $z$  around 0.3, 0.5 and 0.75. Globally, we are selecting less galaxies per redshift bin than we are putting aside. The average and median redshifts are 0.749 and 0.719 for the selected galaxies, 0.809 and 0.750 for the unselected ones. Thus, our sample remains consistent in terms of redshift even after performing the SNR and size selections.

### 2.6.3 Mass-SFR relation

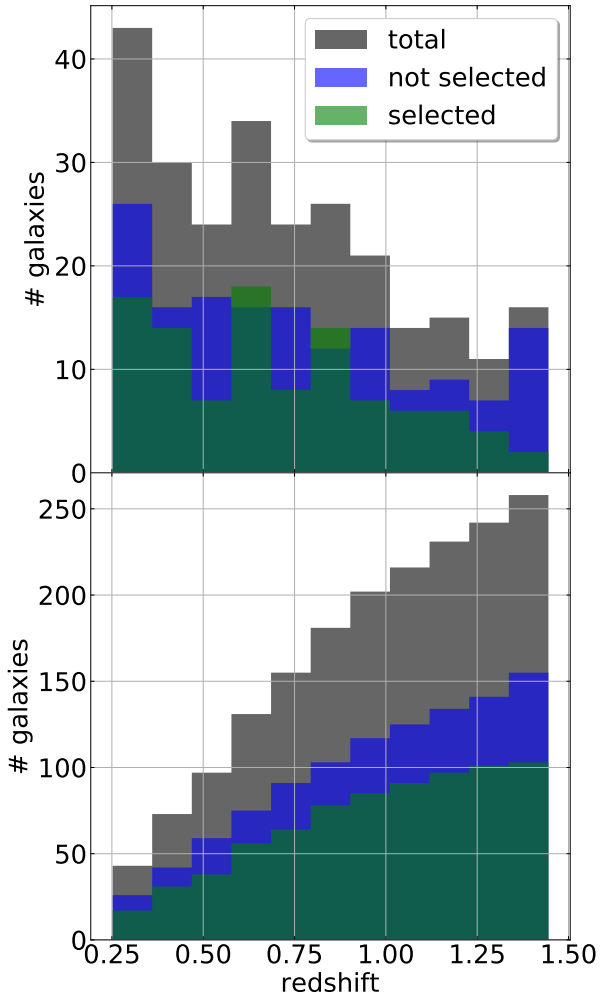


Figure 8: Redshift distribution of the total sample (grey), selected (green) and unselected (blue) galaxies. Redshift bins of size 0.1 have been used. Top: density plot as a function of redshift. Bottom: cumulative distribution. We lack most of the galaxies at redshift 1.4. Other redshift bins do not loose to many galaxies with respect to the unselected ones except maybe at  $z \approx 0.5$ .

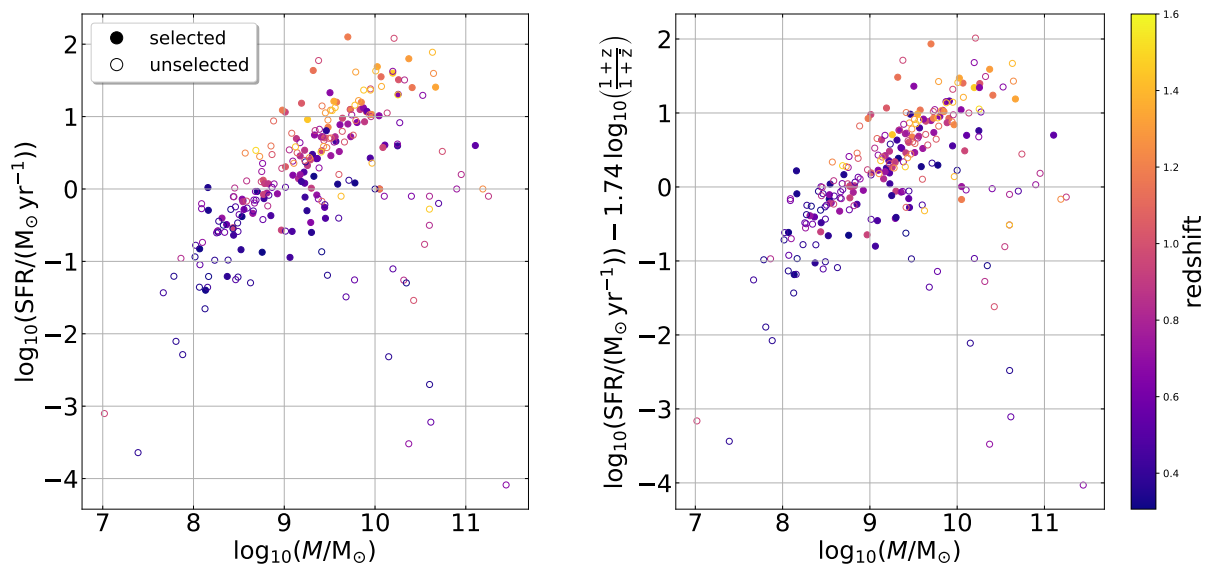


Figure 9: SFR-mass relation for selected (filled circles) and unselected (open circles) galaxies. Left: SFR extracted from the morphological catalogues. Right: the redshift corrected SFR as given in Eq.???. We obtain the usual main sequence of galaxies as a linear relation between SFR and mass (in log-log space), as well as quenched galaxies on the lower right part of the plane which are removed when performing the selection.

### 3 Kinematical modelling

#### 3.1 Cleaning

Before trying to fit a model onto the velocity maps to derive the kinematical parameters of our galaxies, we need to remove any pixel which might be dominated by the noise. Such a cleaning is generally done by keeping pixels whose [OII]  $\lambda\lambda 3729, 3729 \text{ \AA}$  doublet emission line is visually identifiable with respect to the continuum. This quite subjective procedure can be objectified by considering the SNR of each pixel, which is computed in the MUSE pipeline, and by keeping those whose value is above a certain threshold which we chose to be 5.

However, in some cases, we expect to find a strong continuum emission which we may over-interpret as a spectral feature such as [OII]. Continuum emission comes from various physical processes, most being independent from the others, which implies a larger dispersion in the pixels spectra than in the [OII] case. The dispersion threshold above which we consider pixels are noise dominated will depend on the galaxy redshift. Indeed, considering Gaussian line profiles, we find the spectral dispersion as a function of the LSF FWHM of the line by solving  $\exp\{-(\text{FWHM}/2)^2/(2\sigma^2)\} = 1/2$ , i.e.

$$\sigma(z) = \frac{\text{FWHM}}{2\sqrt{2\log 2}} \quad (14)$$

We can explicitly express the redshift dependence by defining an equivalent velocity dispersion  $\sigma_v$  as

$$\frac{\sigma}{\lambda_{\text{em}}(1+z)} = \frac{\sigma_v}{c} \quad (15)$$

This value defines the usual velocity dispersion we expect to measure from the emission line of a galaxy at redshift  $z$ . As the Universe expands ( $z$  going from  $\infty$  to 0), its bulk motion takes over the local movement of matter, reducing the observed dispersion. We decided to choose a velocity dispersion threshold of  $0.8\sigma_v$  for all the galaxies throughout this work.

The cleaning was automatically performed with a routine using both thresholds defined above. Cleaned maps were produced and the velocity maps were visually inspected. Isolated pixels were removed even if they had a clearly visible [OII] doublet. Twelve galaxies were unresolved and 3 were too close to the edges which resulted in missing data. Relaxing the SNR threshold to 3 and removing any pixels on the edges of the galaxies with too weak [OII] emission lines allowed us to recover 6 galaxies out of 12. In the case of resolved galaxies, we also inspected their [OII] doublet near the edges and we removed any pixel whose velocity seemed inconsistent with that of its neighbours (a single negative value around positives ones for instance).

### 3.2 Kinematical parametrisation

The velocity maps we had from the MUSE pipeline only give us information on a fraction of the velocity. Indeed, the velocity of a given pixel is computed using the well known Doppler effect which will redshift pixels going away from us and blueshift those approaching, i.e.

$$\frac{\lambda_{\text{obs}} - \lambda_{\text{em}}}{\lambda_{\text{em}}} = \frac{v}{c} \quad (16)$$

with  $v$  positive if it recedes from us and negative if it approaches. Special relativistic effects being negligible in this case, it means the only measure we have is the radial component of the gas velocity within the pixels. Depending on the basis we choose to decompose our velocity vector, this component will be written differently. In our case, we will use the coordinate system defined in ? (?). Using cylindrical coordinates relative to the galactic plane, we can write the observed projected radial component as

$$V_{\text{obs}}(R, \theta, i, V_{\text{sys}}, \text{PA}) = V_{\text{sys}} + (V_{\text{rot}}(R) \cos \theta + V_{\text{exp}}(R) \sin \theta) \sin i + V_z(R) \cos i \quad (17)$$

where  $V_{\text{obs}}$ ,  $V_{\text{sys}}$ ,  $V_{\text{rot}}$ ,  $V_{\text{exp}}$  and  $V_z$  are the observed, systematic, rotational, expansion and vertical components of the velocity respectively. In practice, spectroscopic measurements give us  $\Delta V_{\text{obs}} = V_{\text{obs}} - V_{\text{sys}}$ . In Eq.17, the dependence on the major axis (kinematical) position angle is implicit as  $\theta$  is defined as the angle in the galactic plane starting from the major axis. Thus,  $\theta = 0^\circ$  ( $90^\circ$ ) when we measure the velocity of a point on the major (minor) axis. The dependence of  $V_{\text{obs}}$  with the radial distance  $R$  to the centre of the galaxy also makes implicit its dependence on the galaxy centre position.

A representation and the definitions of the coordinate system, angles and vector decomposition can be found in Appendix ???. Both  $R$ ,  $\theta$  and the galaxy centre  $(x_c, y_c)$  can be derived from the images, but the inclination of the galaxy must be known in advance. As it will be explained later, models poorly converge when the inclination is let free to vary. Hence, it must be used as a fixed input. More importantly, assuming the rotation curve along the major axis reaches a maximum rotational velocity or at least a plateau, as should be the case in dark matter dominated galaxies (ref here), we see from Eq.17 that the maximum rotational velocity will scale as

$$V_{\text{obs}}^{\text{max}}(R_{\text{max}}, i) = V_{\text{rot}}(R_{\text{max}}) \sin i \quad (18)$$

where  $R_{\text{max}}$  represents the radius at which the maximum velocity or the plateau is reached. Thus, just by looking at the rotation curve and by measuring its maximum value, we cannot raise the degeneracy between the inclination, which will lower the velocity, and the real one. This explains the care taken in checking prior information we had on the  $b/a$  ratio from which is computed the galaxy inclination.

### 3.3 Model

Given the smooth cleaned velocity maps, we can deduce the kinematical parameters of our galaxies by fitting 2D velocity models. Many can be used, but we describe here the one we utilised in this work. We used a parametric model relying on the assumption of a thin disk. This is no longer the case when galaxies are seen nearly edge-on ( $75^\circ \lesssim i \lesssim 90^\circ$ ) due to the increasing depth leading to higher values of opacity. The second assumption is that we can actually model our galaxies with a rotation curve and so that we do not have non-rotational bulk motions. In our case, we assume we have smooth velocity fields with no bar, no arms and no clumps such as HII regions. Nevertheless, based on previous morpho-kinematical studies (ref here), we might expect to find a significant fraction of our galaxies to be dispersion dominated, some with highly perturbed morphologies due to merging in some cases. In our model, 4 morphological and 1 kinematical parameters are used. The inclination of the galaxy, its centre right ascension and declination and the  $PA$  of the major axis must be given as fixed values. The kinematical parameter corresponds to the systematic velocity, that is the radial component of the velocity due to the expansion of the Universe.

## References

- Abraham, R. G., Valdes, F., Yee, H. K. C., & van den Bergh, S. (1994, Sep). The Morphologies of Distant Galaxies. I. an Automated Classification System. *Astrophysical Journal*, *432*, 75. doi: 10.1086/174550
- Abraham, R. G., van den Bergh, S., Glazebrook, K., Ellis, R. S., Santiago, B. X., Surma, P., & Griffiths, R. E. (1996, Nov). The Morphologies of Distant Galaxies. II. Classifications from the Hubble Space Telescope Medium Deep Survey. *Astrophysical Journal Supplement*, *107*, 1. doi: 10.1086/192352
- Bacon, R., Brinchmann, J., Richard, J., Contini, T., Drake, A., Franx, M., ... de Zeeuw, T. (2015, Mar). The MUSE 3D view of the Hubble Deep Field South. *Astronomy and Astrophysics*, *575*, A75. doi: 10.1051/0004-6361/201425419
- Bacon, R., Conseil, S., Mary, D., Brinchmann, J., Shepherd, M., Akhlaghi, M., ... Carollo, M. (2017, Nov). The MUSE Hubble Ultra Deep Field Survey. I. Survey description, data reduction, and source detection. *Astronomy and Astrophysics*, *608*, A1. doi: 10.1051/0004-6361/201730833
- Bershady, M. A., Jangren, A., & Conselice, C. J. (2000, Jun). Structural and Photometric Classification of Galaxies. I. Calibration Based on a Nearby Galaxy Sample. *The Astronomical Journal*, *119*(6), 2645-2663. doi: 10.1086/301386
- Bertin, E., & Arnouts, S. (1996, June). SExtractor: Software for source extraction. *Astronomy and Astrophysics Supplement*, *117*, 393-404. doi: 10.1051/aas:1996164
- Conselice, C. J. (1997, Nov). The Symmetry, Color, and Morphology of Galaxies. *Publications of the Astronomical Society of the Pacific*, *109*, 1251-1255. doi: 10.1086/134004
- Graham, A. W., Driver, S. P., Petrosian, V., Conselice, C. J., Bershady, M. A., Crawford, S. M., & Goto, T. (2005, Oct). Total Galaxy Magnitudes and Effective Radii from Petrosian Magnitudes and Radii. *The Astronomical Journal*, *130*(4), 1535-1544. doi: 10.1086/444475
- Hubble, E. P. (1922, Oct). A general study of diffuse galactic nebulae. *Astrophysical Journal*, *56*, 162-199. doi: 10.1086/142698
- Hubble, E. P. (1926, Dec). Extragalactic nebulae. *Astrophysical Journal*, *64*, 321-369. doi: 10.1086/143018

- Kent, S. M. (1985, Oct). CCD surface photometry of field galaxies. II. Bulge/disk decompositions. *Astrophysical Journal, Suppl. Ser.*, 59, 115-159. doi: 10.1086/191066
- Laigle, C., McCracken, H. J., Ilbert, O., Hsieh, B. C., Davidzon, I., Capak, P., ... Zabl, J. (2016, June). THE COSMOS2015 CATALOG: EXPLORING THE  $1 < z < 6$  UNIVERSE WITH HALF A MILLION GALAXIES. *The Astrophysical Journal Supplement Series*, 224(2), 24. Retrieved 2019-03-21, from <http://stacks.iop.org/0067-0049/224/i=2/a=24?key=crossref.13400bd5b9499f45ce2b1d44c4a48475> doi: 10.3847/0067-0049/224/2/24
- Lotz, J. M., Primack, J., & Madau, P. (2004, Jul). A New Nonparametric Approach to Galaxy Morphological Classification. *The Astronomical Journal*, 128(1), 163-182. doi: 10.1086/421849
- Moffat, A. F. J. (1969, December). A Theoretical Investigation of Focal Stellar Images in the Photographic Emulsion and Application to Photographic Photometry. *Astronomy and Astrophysics*, 3, 455.
- Peng, C. Y., Ho, L. C., Impey, C. D., & Rix, H.-W. (2002, July). Detailed Structural Decomposition of Galaxy Images. *The Astronomical Journal*, 124, 266-293. doi: 10.1086/340952
- Scarlata, C., Carollo, C. M., Lilly, S., Sargent, M. T., Feldmann, R., Kampeczyk, P., ... Takahashi, M. (2007, Sep). COSMOS Morphological Classification with the Zurich Estimator of Structural Types (ZEST) and the Evolution Since  $z = 1$  of the Luminosity Function of Early, Disk, and Irregular Galaxies. *The Astrophysical Journal Supplement Series*, 172(1), 406-433. doi: 10.1086/516582
- Schade, D., Lilly, S. J., Crampton, D., Hammer, F., Le Fevre, O., & Tresse, L. (1995, Sep). Canada-France Redshift Survey: Hubble Space Telescope Imaging of High-Redshift Field Galaxies. *Astrophysical Journal Letters*, 451, L1. doi: 10.1086/309677
- Scoville, N., Aussel, H., Brusa, M., Capak, P., Carollo, C. M., Elvis, M., ... Tyson, N. D. (2007, Sep). The Cosmic Evolution Survey (COSMOS): Overview. *The Astrophysical Journal Supplement Series*, 172(1), 1-8. doi: 10.1086/516585
- Sérsic, J. L. (1963). Influence of the atmospheric and instrumental dispersion on the brightness distribution in a galaxy. *Boletín de la Asociacion Argentina de Astronomia La Plata Argentina*, 6, 41.
- Simard, L. (1998, Jan). GIM2D: an IRAF package for the Quantitative Morphology Analysis of Distant Galaxies. In R. Albrecht, R. N. Hook, & H. A. Bushouse (Eds.), *Astronomical data analysis software and systems vii* (Vol. 145, p. 108).

Swinbank, A. M., Harrison, C. M., Trayford, J., Schaller, M., Smail, I., Schaye, J., ... Stott, J. P. (2017, May). Angular momentum evolution of galaxies over the past 10 Gyr: a MUSE and KMOS dynamical survey of 400 star-forming galaxies from  $z = 0.3$  to 1.7. *Monthly Notices of the Royal Astronomical Society*, 467(3), 3140-3159. doi: 10.1093/mnras/stx201



## A Details about morphological classification

We provide in this section a summary of the morphological parameters used by Cassata, Tasca and Zurich for their morphological classification which we used and compared in the present work.

### A.1 Non-parametric values

Usual galaxy classification methods rely on the same parameters. Some may use all of them when others only concentrate on a few. We give here a description of the main parameters used for this kind of classification.

#### A.1.1 Concentration

The first parameter is the concentration. Two quite different definitions exist, the former using flux levels and the latter isophotes. The oldest definition of the concentration comes from Kent (1985). In his paper, he describes it as the log of the ratio between the radii enclosing 80% and 20% of the "total" luminosity (respectively  $r_{80}$  and  $r_{20}$ )

$$C = 5 \log \frac{r_{80}}{r_{20}} \quad (19)$$

The concentration parameter can vary in theory from 1 to infinity. The parameter  $C$  as defined in Eq. 19 should be interpreted cautiously as many definitions of the "total" luminosity (sometimes also called total flux) are used. Some authors who have performed a morphological modelling might call total luminosity the integrated flux up to infinity of their best fit model. Others might use the flux within some fixed aperture (generally a multiplicative factor of the Petrosian radius  $r_p$ ), such as  $2r_p$  in Bershady et al. (2000), or  $1.5r_p$  in Lotz et al. (2004).

Another definition comes from Abraham et al. (1994). In this case, second order moments of the image are computed in order to find an outer elliptical aperture with an area similar to that of the galaxy up to some isophotal limit (generally  $2\sigma$ ). From this ellipse, the semi-major axis can be obtained. A second semi-major axis 30% smaller is derived and an inner ellipse with the same shape is defined. The concentration parameter is then computed as the ratio between the flux within the outer and the inner apertures

$$C = \frac{\sum_{(x,y) \in \mathcal{E}_{\text{in}}} I(x,y)}{\sum_{(x,y) \in \mathcal{E}_{\text{out}}} I(x,y)} \quad (20)$$

where  $\mathcal{E}_{\text{in}}$  and  $\mathcal{E}_{\text{out}}$  are respectively the inner and outer ellipses. This definition therefore yields a concentration parameter  $C$  between 0 and 1.

### A.1.2 Asymmetry

The asymmetry parameter defines how symmetric/asymmetric a galaxy is. A related parameter was first introduced by Schade et al. (1995) in order to classify galaxies as being symmetric or not, though its definition differed by using a combination of original and residual maps in its computation.

The most common definition of the asymmetry  $A$  comes from Abraham et al. (1996). The map is rotated by  $180^\circ$  and is subtracted to the original map. The asymmetry parameter is then computed as half the ratio between the total integrated intensity amplitude in the self-subtracted map and the total intensity amplitude in the original map. Using an absolute value will add a positive term in  $A$  from background signal. To get rid of it, the same calculation is performed for an aperture of the same size with only background signal and this value is subtracted from the previous one, i.e.

$$A = \frac{\sum_{i,j} |I(i,j) - I_{180}(i,j)|}{2 \sum_{i,j} |I(i,j)|} - B_{180} \quad (21)$$

where  $I_{180}$  designates the rotated map and  $B_{180}$  is the average asymmetry of the background. This definition, though commonly used, is sometimes replaced by a similar one where square brackets are used instead of absolute values. This is for instance the case in Conselice (1997). Nevertheless, both definitions yield values of  $A$  between 0 (completely symmetrical) and 1 (completely asymmetrical).

The value of  $A$  can be quite sensitive to the choice of the centre. Methods for finding the best centre position include using the brightest point in a smoothed map or iterating over  $X$  and  $Y$  till  $A$  is minimised.

### A.1.3 Gini coefficient